Giant isolated half-cycle attosecond pulses generated in coherent bremsstrahlung emission regime

Qing Xin,[1] Yunliang Wang,[1,*] Xueqing Yan,[2,3,4,†] and Bengt Eliasson[5,‡]

[1]Department of Physics, School of Mathematics and Physics, University of Science and Technology Beijing, Beijing 100083, China
[2]State Key Laboratory of Nuclear Physics and Technology, and Key Laboratory of HEDP of the Ministry of Education, CAPT, Peking University, Beijing 100871, China
[3]Beijing Laser Acceleration Innovation Center, Beijing 100871, China
[4]Collaborative Innovation Center of Extreme Optics, Shanxi University, Shanxi 030006, China
[5]SUPA, Physics Department, John Anderson Building, University of Strathclyde, Glasgow G4 0NG, Scotland, United Kingdom

(Received 16 November 2022; revised 14 December 2022; accepted 16 February 2023; published 6 March 2023)

Giant half-cycle attosecond pulse generation in the coherent bremsstrahlung emission regime is proposed for laser pulses with normal incidence on a double-foil target, where the first foil is transparent and the second foil is opaque. The presence of the second opaque target contributes to the formation of a relativistic flying electron sheet (RFES) from the first foil target. After the RFES has passed through the second opaque target, it is decelerated sharply, and bremsstrahlung emission occurs, which results in the generation of an isolated half-cycle attosecond pulse having an intensity of $\sim 1.4 \times 10^{22}$ W/cm^2 and a duration of 3.6 as. The generation mechanism does not require extra filters and may open a regime of nonlinear attosecond science.

DOI: 10.1103/PhysRevE.107.035201

I. INTRODUCTION

Ultrafast attosecond science has developed rapidly due to the huge potential of providing unprecedented temporal and spatial resolution for the detection of ultrafast atomic and electronic phenomena [1–3]. The high-order harmonic generation (HHG) through laser-plasma interaction has been shown to be an effective way of obtaining ultrahigh-amplitude attosecond pulses (APs) [4,5].

Based on the extremely compact electron accelerator in the laser-plasma interaction, relativistic electron bunches are a powerful approach for producing extreme ultraviolet and x-ray laser pulses [6–8]. The laser interactions with a solid target can generate extremely dense nanometer-scale electron sheets, which are accelerated to an ultrarelativistic velocity at the stationary phase point where the AP is emitted in a coherent synchrotron emission (CSE) regime [6,9–15].

The relativistic electron sheets (RESs) are formed periodically twice per cycle due to the combined action of the Lorentz and Coulomb forces [9]. This leads to a train of intense attosecond XUV and x-ray pulses emitted by the RES. However a single isolated AP is preferred for many applications [16–20]. Many efforts have been devoted to the generation of single APs, such as polarization gating [21–27] and ionization gating [28,29], two-color driven laser pulses [30], few-cycle driven laser pulses [31–33], etc.

The laser pulse interaction with double-target scheme is also useful to produce isolated APs [34–36], where the first foil target is transparent and the second foil target is opaque. Accordingly, the laser pulse can penetrate the first foil target and is incidence on the second target. When the RES formed from the first target collides with the laser pulse reflected from the second target in the gap of the double targets separated by a distance of 140 nm, a single AP can be generated in the transmitted direction [34]. If the length of the gap is reduced to 60 nm with other laser-plasma parameters unchanged, another RES is formed from the second, thicker target and generates a single AP in the reflected direction. In both cases, the electron nanobunch from the first foil target disperses when it penetrates the second foil target, and neither of these two single APs is a half-cycle pulse [34,35]. For oblique incidence of an *s*-polarized laser pulse on the double target, the RES can be achieved from the first ultrathin foil by the blowout regime. As the thickness and density of the second foil target in the oblique incidence case are much smaller than those in the abovementioned case [34,35], the RES from the first foil target does not disperse but pass through the second foil, where the RES gains a momentum perpendicular to the direction of polarization due to the transverse kick effects from the reflected lase pulse [36]. A giant half-cycle AP is emitted in the transmitted direction when the RES emerges from the second foil [36]. If the laser pulse is normally incident on the double-foil target, the transverse kick will not occur in the direction perpendicular to the direction of polarization. Accordingly, the corresponding transverse current is absent, and the AP is no longer emitted, as analyzed by theoretical analysis [36] and confirmed by experiment [37].

However, in this paper we will show that a giant half-cycle AP can also be generated by a laser pulse with normal incidence on a double-foil target in a coherent bremsstrahlung emission (CBE) regime. The second opaque target is no longer used as a reflection target in our case. The relativistic electron nanobunch formed by the first foil target can be continuously

*ylwang@ustb.edu.cn
†x.yan@pku.edu.cn
‡bengt.eliasson@strath.ac.uk

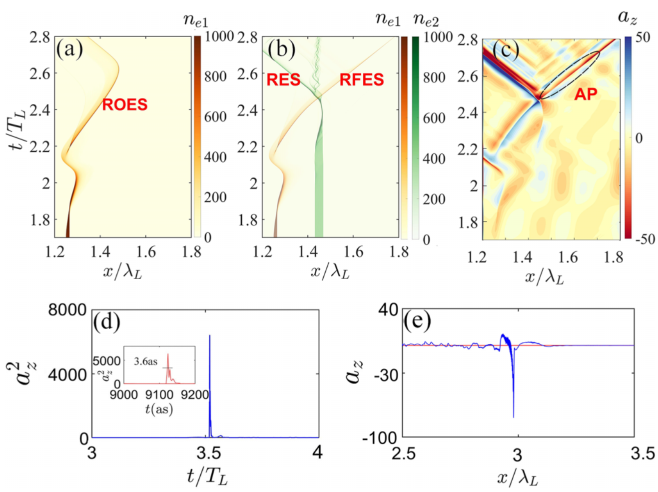

FIG. 1. (a) The dynamics for the electron density n_{e1} of the ROES without the second foil target. (b) The dynamics of the RFES (n_{e1}) and the RES (n_{e2}) in the double-foil target case. (c) The spatiotemporal evolution of the normalized electric field a_z, where the electric field of the AP is marked by a black ellipse. (d) The intensity profile of the AP. The inset shows a FWHM of about 3.6 as. (e) The electric field of the AP shows approximately a half-cycle profile.

accelerated to ultrarelativistic velocity in the gap between the two foils and will be sharply decelerated on the rear side of the second foil target, which results in the generation of half-cycle APs. The half-cycle pulses are useful for the excitation of vibrational levels in polar molecules [38], electron and nuclear joint dynamics [39], and electron dynamics through asymmetrical manipulation [40]. Our CBE regime based on the double-foil target scheme has great simplicity and potential.

II. THE COHERENT BREMSSTRAHLUNG EMISSION REGIME OF APs

Here, we highlight a regime of attosecond pulse generation by coherent bremsstrahlung emission (CBE), where a half-cycle AP is emitted by a laser pulse with normal incidence on a double-foil target. Here, the first foil target is transparent, and the second foil target is opaque. For normal incidence of the laser pulse linearly polarized along the z direction on the first foil target, the radiation pressure pushes the electron layer forwards, which forms a relativistic oscillating electron sheet (ROES) as shown in Fig. 1(a) in the absence of a second foil target. However, in the presence of a second foil target, the laser pulse penetrating the first foil target will be reflected back by the second target, which greatly enhances the Lorentz force. As a result, the second opaque-foil target switches the relativistic electron nanobunch from ROES to a relativistic flying electron sheet (RFES) as shown in Figs. 1(a) and 1(b). The RFES is accelerated to ultrarelativistic velocity in the gap of the two foils. When the transmitted laser pulse preceding the RFES interacts with the second foil, a relativistic electron sheet (RES) from the second foil is formed and accelerated in the opposite direction, which results in a huge electrostatic field (~100 TV/m) due to the charge separation. After the RFES transits the second foil target, the RFES are decelerated sharply by the huge electrostatic field, and a bremsstrahlung emission occurs, which leads to the generation of a half-cycle AP as shown in Fig. 1(c). In Fig. 1(d), the giant isolated half-cycle AP has a squared amplitude of $a_z^2 \approx 6835$ and a corresponding intensity of 1.46×10^{22} W/cm^2. The full width at half maximum (FWHM) of the AP is about 3.6 as. As seen in Fig. 1(e), the AP is approximately a half-cycle pulse. Even though the transmitted half-cycle AP is produced by the RFES formed from the first foil target, the second foil target plays an important role for our CBE regime. In the oblique incidence case, the second foil target is mainly used as a reflection target to achieve the transverse kick [36,37]. However, in our case the second target has two roles: (a) When the RFES moves forward in the gap between the two foils, it is continuously accelerated to ultrarelativistic velocity as a result of the reflected laser pulse from the second foil target. (b) When the RFES moves on the rear side of the second foil, the RFES obtains a great deceleration due to the huge Coulomb field of $E_x \sim 100$ TV/m, which is created by the second foil target.

This CBE regime of giant half-cycle AP generation is simulated by the particle-in-cell code EPOCH [41]. The two-color laser pulses have a Gaussian temporal envelope given by $a_{z1,2} = a_{01,02} e^{-(t-T_L)^2/\tau^2} \sin[\omega_{1,2}(t - T_L) + \phi_{1,2}]$, where $\phi_1 = 4.607$ rad, $\phi_2 = 5.909$ rad, and $\tau = 0.5T_L$. The angular frequency is $\omega_L = 2\pi c/\lambda_L$, and the period is $T_L = \lambda_L/c$ for $\lambda_L = 800$ nm. Here, $\omega_1 = \omega_L$ and $\omega_2 = 2\omega_L$. The amplitudes are $a_{01} = 65$ and $a_{02} = 65$, and the corresponding intensities are 9.2×10^{21} and 3.7×10^{22} W/cm^2. The amplitude is normalized as $a_z = eE_L/(\omega_L m_e c)$ with E_L being the electric field amplitude, m_e being the electron rest mass, e being the unit charge, and c being the speed of light in a vacuum. The length of the one-dimensional simulation box is $5\lambda_L$, which is resolved by 10 000 cells per wavelength. The thicknesses of the first foil target d_1 and second foil target d_2 are 12 and 30 nm, respectively. The first foil target is located at $1.25\lambda_L < x < 1.265\lambda_L$ with density $n_{e1} = 966n_c$. The second foil target is located at $1.431\,25\lambda_L < x < 1.468\,75\lambda_L$ with density $n_{e2} = 545n_c$, where $n_c = \omega_L^2 \epsilon_0 m_e/e^2$ is the critical density with ϵ_0 being the dielectric constant in the vacuum.

We here discuss the rationality and necessity of the above laser-plasma parameters used in the particle-in-cell simulations. As we aimed to achieve ultraintense APs, the density of the first foil target needs to be so high that the charge of the RFES is high enough. The thickness of the first foil target needs to be thin enough to form the RFES in the blowout regime, because the peak amplitude a_z of the laser pulse should be larger than the normalized maximum electrostatic force $a_z \geqslant \pi n_{e1} \frac{d_1}{\lambda_L}$ due to the charge separation [34,42,43]. The thickness and density of the second target must also be such that the maximum depletion length is approximately equal to its thickness when the whole second target is compressed by the penetrating laser pulse. Only in this way can the electrons of the second foil target be pulled out completely by the combined effects of laser ponderomotive force and the electrostatic force. Then another RES from the second foil is formed and accelerated in the opposite direction, which results in a huge electrostatic field (~100 TV/m) due to the charge separation. The initial phase used here is useful for a driven laser pulse to have an extremely steep front rising to peak

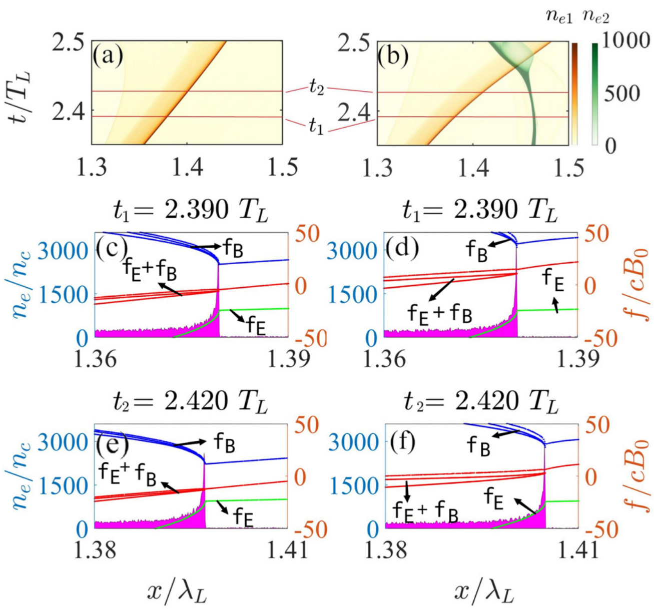

FIG. 2. Left column: (a) In the case of the single-foil target, a close-up of the spatiotemporal evolution of electron density n_{e1} of ROES. (c) and (e) show the Coulomb force f_E (green dotted line), the Lorentz force f_B (blue dotted line), and the resultant force $f_E + f_B$ (red dotted line) acting on ROES at $t = 2.390T_L$ and $t = 2.420T_L$, respectively. Right column: (b) In the case of the double-foil target, a close-up of the spatiotemporal evolution of electron density n_{e1} of RFES and n_{e2} of RES. As the RFES moves in the vacuum gap between the two foils, (d) and (f) show the Coulomb force f_E (green dotted line), the Lorentz force f_B (blue dotted line), and the resultant force $f_E + f_B$ (red dotted line) acting on RFES at $t = 2.390T_L$ and $t = 2.420T_L$, respectively. The pink-shaded areas in (c)–(f) stand for the position of the RFES.

intensity, which can blow out a major part of the electrons in the first foil target and contribute to the formation of RFES with extremely high density.

Figure 2 illustrates a comparison of simulation with and without the second foil target, while keeping other parameters unchanged. In the absence of a second foil, the driven laser pulse interacts with the first transparent foil and then blows out the majority of the electrons of the first foil. The Coulomb restoring force due to the displacement of the electrons increases and pulls them back when the Lorentz force decreases, which results in a relativistic oscillation and the formation of the ROES as shown in Fig. 1(a). Similar ROESs have been analyzed in detail for AP generation in the CSE regime [43]. We select the times $t = 2.390T_L$ and $t = 2.420T_L$ to show the resultant Coulomb and Lorentz forces $f_E + f_B$ [represented by red dots in Figs. 2(c) and 2(e)] acting on the ROES. Because the Coulomb force is larger than the Lorentz force, the resultant force is negative and pulls the ROES back to the reflected direction. The electrodynamics is determined by the normalized areal charge density $\sigma_1 = \pi n_{e1} d_1/\lambda_L \sim 45.50$, where n_{e1} and d_1 are the density and thickness of the first foil, respectively [44]. As the normalized maximum amplitude $a_0 \sim 116$ is larger than the areal charge density $\sigma_1 \sim 45.5$, the first foil is a transparent target. Accordingly, the laser pulse can penetrate the first foil target and is normally incident on the second foil target.

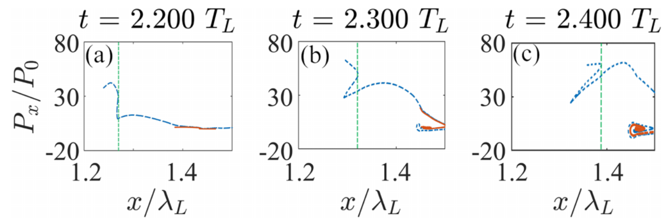

FIG. 3. The electron longitudinal momentum distribution in the x-p_x plane at different times $t = 2.200T_L$ (a), $t = 2.300T_L$ (b), and $t = 2.400T_L$ (c). The red dotted line indicates electrons from the second foil target, and the blue dashed line indicates electrons from the first foil target. Momentum $P_x = \gamma m_e v_x$ is normalized by $P_0 = m_e c$. The green dashed line stands for the positions of the RFES at different times.

By contrast, at the time $t = 2.390T_L$ and $t = 2.420T_L$ the resultant force $f_E + f_B$ [represented by red dots in Figs. 2(d) and 2(f)] acting on the relativistic electrons is positive in the presence of the second foil target, which is due to the fact that the second foil is an opaque target that reflects the laser pulse and greatly enhances the Lorentz force. The areal charge density of the second foil $\sigma_2 = \pi n_{e2} d_2/\lambda_L \sim 64$ is larger than the amplitude of the laser pulse $a_z \sim 57$. Accordingly, the resultant force is always positive, although the Coulomb force is negative as shown in Figs. 2(d) and 2(f). Then the RFES can be continuously accelerated to ultrarelativistic velocity when the RFES moves in the vacuum gap between the two foil targets, which is confirmed in Fig. 3. We can see that the longitudinal momentum of the RFES increases continuously from $t = 2.200T_L$ to $t = 2.400T_L$ as shown in Fig. 3. As a result, the second opaque-foil target switches the relativistic electron nanobunch from ROES to RFES as shown in Figs. 1(a) and 1(b).

After the RFES has transited the second opaque-foil target, the RFES will be sharply decelerated. As the laser pulse is reflected by the second opaque-foil target, the Lorentz force f_B [represented by blue dots in Figs. 4(b)–4(d)] acting on the RFES is close to zero. The resultant force $f_E + f_B$ [represented by red circles in Figs. 4(b)–4(d)] acting on the RFES is dominated by the Coulomb force f_E [represented by green pluses in Figs. 4(b)–4(d)], which is very large as the electrostatic field is ∼100 TV/m as shown in Figs. 4(h)–4(j). The longitudinal momentum of the RFES decreases sharply due to the deceleration as shown in Figs. 4(e)–4(g). The half-cycle AP is emitted by the RFES during the deceleration in the CBE regime as shown in Figs. 4(h)–4(j). It should be pointed out that the self-action electric and magnetic field acting on the RFES increases the resultant external force acting on the RFES, which has an enhanced deceleration effect by the self-action effects, as shown in Figs. 4(b)–4(d). We can see in Figs. 4(b)–4(d) that the negative Lorentz force f_B increases rapidly with the increase of the amplitude of the emitted AP.

Here we discuss the propagation and description of the half-cycle AP. In Fig. 5, we illustrate the propagation properties of the AP, which shows that the shape of the half-cycle

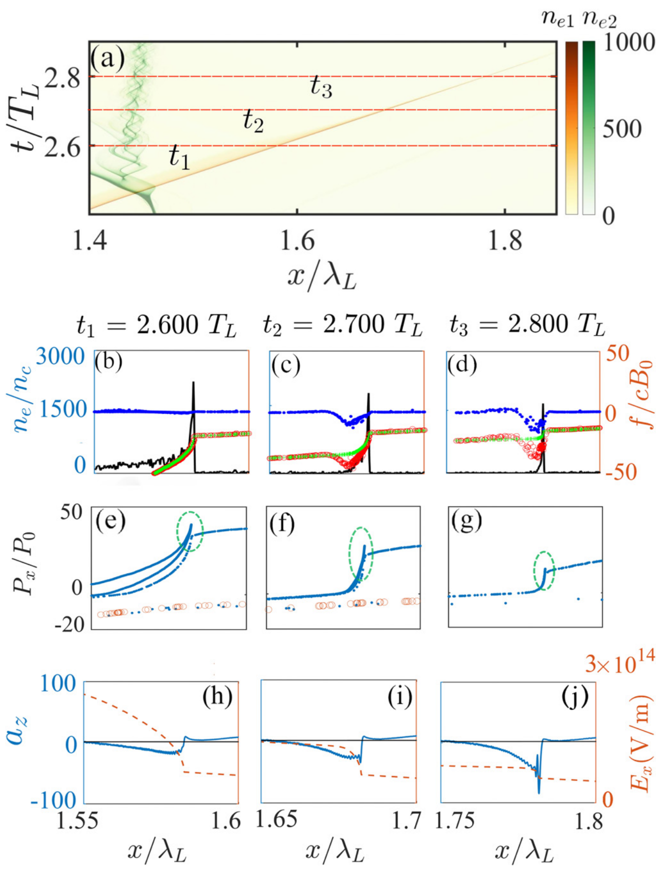

FIG. 4. (a) In the case of the double-foil target, a close-up of the spatiotemporal evolution electron number density n_{e1} and n_{e2} that is normalized by n_c when the RFES moves behind the second foil target. (b)–(d) show the Coulomb force f_E (green pluses), the Lorentz force f_B (blue dots), and the resultant force $f_E + f_B$ (red circles) acting on the RFES at $t = 2.600T_L$, $t = 2.700T_L$, and $t = 2.800T_L$, respectively. The black solid lines in (b)–(d) show the profile of the electron density of the RFES. (e)–(g) show the electron longitudinal momentum distribution in the x-p_x plane at different times $t = 2.600T_L$, $t = 2.700T_L$, and $t = 2.800T_L$, respectively. (h)–(j) show the profile of the AP (blue solid line) and the electrostatic field E_x (red dashed line) at different times $t = 2.600T_L$, $t = 2.700T_L$, and $t = 2.800T_L$, respectively.

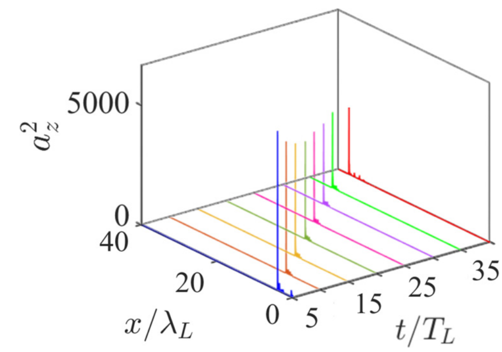

FIG. 5. The evolution of the half-cycle AP is illustrated at different times $t = 5T_L$, $t = 10T_L$, $t = 15T_L$, $t = 20T_L$, $t = 25T_L$, $t = 30T_L$, $t = 35T_L$, and $t = 40T_L$ when it propagates in a vacuum.

AP remains roughly unchanged except that its amplitude decreases slightly with time during propagation. Then one can conclude that the half-cycle AP can propagate stably in the vacuum for dozens of cycles in the transmitted direction. For simplicity, the half-cycle AP can be modeled by a delta function in time. A more realistic model temporal profile is a Gaussian temporal profile $\exp(-t^2/\tau_d^2)$ or sine-square temporal profile $\sin^2(\pi t/\tau_d)$ for $0 < t < \tau_d$, where τ_d is the pulse width [40]. From Fig. 1(e), we can see that the half-cycle AP has a strong asymmetric oscillation with a much weaker and long tail of the opposite polarity, which can be described by the following function: $(t/\tau_0)[\exp(-t^2/2\tau_0^2) - b^{-2}\exp(-t/b\tau_0)]$ for $t > 0$. Here, τ_0 and b determine the duration and the asymmetry of the half-cycle AP, respectively [45].

III. THEORETICAL ANALYSIS OF THE HALF-CYCLE AP

Here we discuss the coherent condition in our CBE regime. The intensity spectrum for N electrons in the electron nanobunch is given by $dI/d\omega_N = (dI/d\omega_1)[N + N(N-1)\widetilde{n}_{e1}(\omega)]$ [12], where $dI/d\omega_1$ is the intensity per spectral bandwidth of one electron and $\widetilde{n}_{e1}(\omega)$ is the Fourier transform of the electron density profile of the RFES. The central wavelength of the half-cycle AP is ~40 nm according to our simulation results. The corresponding coherence length is about $l_c < \frac{\lambda}{2} \sim 20$ nm. The longitudinal electron bunch length of the RFES is about $l_b = 0.237$, 0.233, and 0.199 nm at time $t = 2.6T_L$, $2.7T_L$, and $2.8T_L$ during the bremsstrahlung emission of the AP as shown in Figs. 4(b)–4(d). As the longitudinal length of RFES is much smaller than the coherence length $l_b \ll l_c$, the $\widetilde{n}_{e1}(\omega)$ is nonzero, and the emission from the entire RFES can be coherent superposition [12].

The self-action electromagnetic field acting on the RFES can be obtained by the thin foil model as [44]

$$E_z = \sigma_1 \frac{v_z}{1 - v_x^2}. \tag{1}$$

The transverse dynamics of the RFES is determined by $dp_z/dt = -E_z$. Considering that $\gamma_x = (1 - v_x^2)^{-1/2}$ and $v_z = p_z/\gamma$, the transverse dynamics of the RFES can be determined by

$$\frac{dp_z}{dt} = -\sigma_1 \frac{\gamma_x^2}{\gamma} p_z, \tag{2}$$

which gives that the transverse momentum p_z will decay exponentially on a timescale $\tau \sim (\sigma_1\gamma_x^2/\gamma)^{-1}$. Here, the dimensionless variables with time and space are normalized by ω_L and c/ω_L, respectively. The electric field and plasma density are normalized by $m_e\omega_L c/e$ and $m_e\omega_L^2/4\pi e^2$, respectively. Here, the normalized areal charge density is $\sigma_1 \sim 45.5$. We can obtain the relativistic factor $\gamma_x \sim 10$, and $\gamma \sim 30$ from the simulation as shown in Fig. 6(a). Accordingly, the emitted pulse will decay on the timescale ~2.8 as, and the corresponding FWHM is ~3.3 as, which is close to the 3.6 as of the simulation results in Fig. 1(d).

The spectrum of the transmitted half-cycle AP depends on the normalized (by en_cc) transverse current

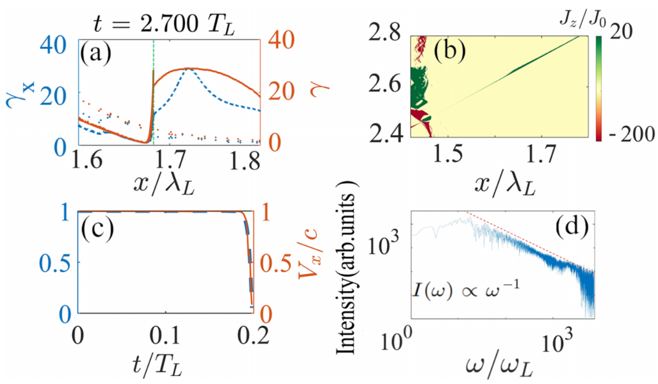

FIG. 6. (a) The relativistic factor γ_x and the full relativistic factor γ are illustrated by blue dashed line and red dotted line, respectively. The green dashed line stands for the positions of the RFES. (b) The transverse current density of the RFES, normalized by $J_0 = n_c ec$. (c) The longitudinal velocity v_x of the RFES as a function of time. The red solid line shows the simulation results. The blue dashed line is the fitted curve with $v_x = v_0 - b_n t^{2n}$ for $v_0 \sim 1$, $n = 30$, and $b_n = 1.5 \times 10^{42}$. (d) The harmonic spectra of the half-cycle AP. The attenuation of the spectrum follows $I(\omega) \propto \omega^{-1}$.

$J_z(x,t) = -v_z(t)n_{e1}(x - x_0(t))$ as [11,43]

$$E(\omega) = -\pi \iint v_z(t+x')n_{e1}[x' - X_0(t+x')]e^{-i\omega t}\,dx'dt. \tag{3}$$

The structure of the spectrum of $E(\omega)$ depends on the position $X_0(t)$ of the RFES. From Fig. 6(c), we can assume that the velocity of the RFES is $v_x(t) = v_0 - b_n t^{2n}$. The larger n is, the better the curve fits. Accordingly, the position of the RFES is $X_0(t) = v_0 t - b_n t^{2n+1}/(2n+1)$. From the approximation $v_x^2 + v_z^2 = v^2$ [11], we can obtain the transverse velocity as $v_z = -(2vb_n)t^n$, which is consistent with the simulation results as shown in Fig. 6(b). Now we can obtain the spectrum of the half-cycle AP as

$$I(\omega) = 8\pi^4 v\omega^{-1}\left|\mathrm{Ai}_n^{(n)}(\xi)\right|^2 |\tilde{n}_{e1}(\omega)|^2, \tag{4}$$

where $\xi = (v_0 - 1)\omega^{\frac{2n}{2n+1}}(-b_n)^{-\frac{1}{2n+1}}$. $\omega^{-\frac{2n}{2n+1}}$ can be approximated as ω^{-1} for large n. $\mathrm{Ai}_n^{(n)}(\xi) = (1/2\pi)\int \tau^n e^{i\xi\tau} e^{i\tau^{(2n+1)}/(2n+1)} d\tau$ is the nth derivative of the generalized Airy function [11], and $\tilde{n}_{e1}(\omega)$ is the Fourier transform of the density shape distribution of the RFES. The spectrum of harmonics is shown in Fig. 6(d). The above theoretical prediction confirms the $I(\omega) \propto \omega^{-1}$ scaling law in the spectrum.

IV. ROBUSTNESS OF THE HALF-CYCLE AP GENERATION IN THE CBE REGIME

We have performed a series of simulations to verify the robustness of the half-cycle AP generation in the CBE regime from the double-foil target scheme with different laser and double-foil target conditions.

A. The robustness to the target parameters

The half-cycle AP is generated by the RFES, which was formed by the first foil target. The electrodynamics of the first foil target can be analyzed by the normalized areal charge density [44]

TABLE I. The effect of the density and the thickness of the first foil target on half-cycle AP generation.

d_1 (nm)	n_{e1}	a_z^2	FWHM (as)	I (10^{22} W/cm^2)
7	1656	5527	5.7	1.18
8	1449	6698	3.7	1.43
9	1288	6476	3.8	1.38
10	1159	5154	6.3	1.10
11	1054	5066	5.2	1.08
12	966	6835	3.5	1.46
13	892	4967	6.3	1.06
14	828	4351	6.4	0.93
15	773	5864	3.9	1.25
16	725	5455	4.2	1.16

$$\sigma_1 = \pi n_{e1}\frac{d_1}{\lambda_L}, \tag{5}$$

where n_{e1} is normalized by n_c. We can also expect that the electrodynamics of the RFES will be similar when the density and the thickness of the first foil target change simultaneously to ensure that their product $n_{e1}d_1$ is unchanged. We have performed a series of simulations to verify the similarity of the electrodynamics of the RFES by changing the density and thickness of the first foil target. The simulation results are listed in Table I. The first column of Table I shows the thickness of the first foil target, from 7 to 16 nm, and the second column represents the density of the first foil target. The unchanged normalized areal charge density is $\sigma_1 \sim 45.50$ in all cases. We can see that the durations of the AP are all below 7 as and the intensity $I > 0.9 \times 10^{22}$ W/cm^2 for all cases. As long as the normalized areal charge density is roughly the same, our unique CBE regime can always produce isolated half-cycle APs with ultrahigh amplitude.

We also investigated the robustness for different parameters related to the second foil target. We explored the effect of the density of the second foil target on the AP generation by keeping the other parameters unchanged. As shown in Fig. 7(a), the density of the second foil target is between $537n_c$ and $565n_c$, which can support the generation of the AP. The duration of the AP is below 6 as, and the intensity is $a^2 > 4000$. Figure 7(b) shows the effects of the distance l between the two foils on the AP. If the distance is in the range

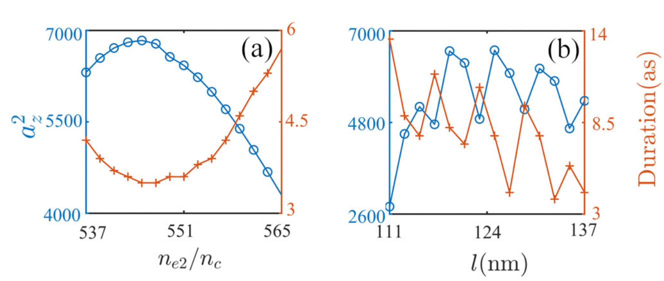

FIG. 7. Durations (attoseconds) at FWHM and normalized intensities for different second-foil densities (a) and for different distances between the two foils (b).

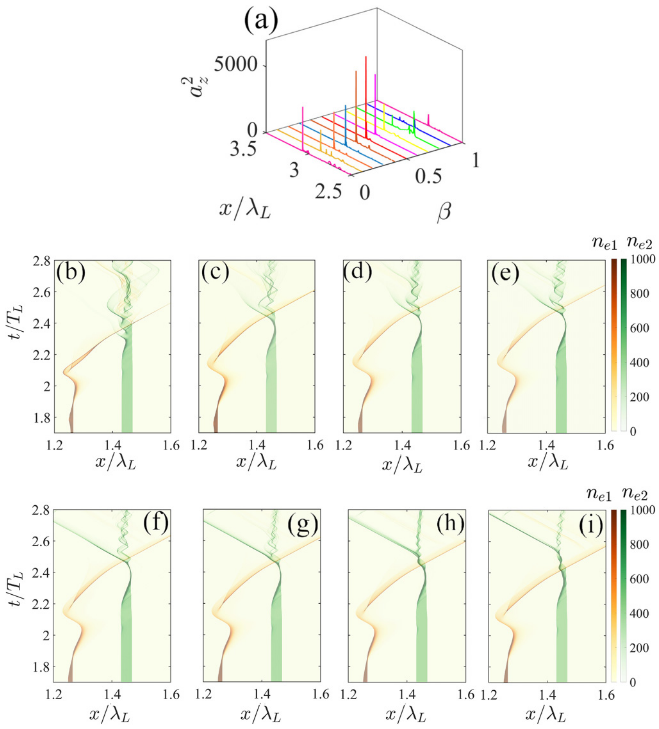

FIG. 8. (a) The profile of the intensity of the half-cycle AP for the energy ratio in the range $\beta \approx 0$–1. The space-time evolution of the electron number density n_e/n_c for different energy ratios: (b) $\beta = 0$, (c) $\beta = 0.1$, (d) $\beta = 0.2$, (e) $\beta = 0.3$, (f) $\beta = 0.4$, (g) $\beta = 0.5$, (h) $\beta = 0.6$, and (i) $\beta = 0.7$.

111 nm $< l <$ 137 nm, the half-cycle AP is always generated with the durations all being below 14 as.

B. The robustness to the laser pulse parameters

We also verify the robustness of our CBE regime in relation to the two-color laser pulse parameters. In our case, the two-color laser pulses are useful for enhancing the half-cycle AP generation yield. To explore the effect of the two-color laser pulse on generation of the AP under different conditions, we focused on the energy ratio and the relative phase between the fundamental-frequency and second-harmonic-frequency laser pulses.

We first discuss the effect of the energy ratios of the two laser pluses on the AP. The amplitudes of the fundamental-frequency and second-harmonic-frequency laser pulses are a_1 and a_2, respectively. We change a_1 and a_2 on the premise that the relationship $a_1^2 + a_2^2 = a_0^2$ is always satisfied. Here, $a_0^2 = a_{01}^2 + a_{02}^2$ is a constant determined by $a_{01} = a_{02} = 65$. If we set $\beta = a_2^2/a_0^2$, which represents the ratio of the second-harmonic energy to the total energy, we can obtain that $a_1 = \sqrt{1-\beta}a_0$ and $a_2 = \sqrt{\beta}a_0$. It can be seen from the simulation that a half-cycle AP can be obtained with the energy ratio in the range $\beta \approx 0$–0.8 as shown in Fig. 8(a). The optimal energy ratio is $\beta = 0.5$ as illustrated by the red line in Fig. 8(a), which shows that the amplitude and duration of the AP are approximately 82 and 3.6 as, respectively.

We can conclude that the AP can still be effectively generated with only fundamental-frequency laser pulses normally incident on the double-foil target. However, the enhancement of the intensity of the half-cycle AP is achieved with the addition of the second-harmonic laser pulses. The physical mechanism for the one-color laser pulse case is exactly the same as that of the two-color laser pulse case, which is illustrated by the pink line at $\beta = 0$ in Fig. 8(a). The formation mechanism of the RFES with only the fundamental-frequency laser pulse is identical to the case of the two-color laser pulse. Accordingly, the mechanism of the half-cycle AP generation is very similar for both the one-color laser pulse case and the two-color laser pulse case.

In order to illustrate the electrodynamics of the RFES intuitively for different energy ratios, we also give the spatiotemporal evolution of the electron number density n_{e1} and n_{e2} in Figs. 8(b)–8(i). For all cases, the electrodynamics of the first foil target is very similar. As the laser pulses irradiate with normal incidence on the first foil target, the radiation pressure pushes the electron layer forwards to form the RFES. For the optimal energy ratio of $\beta = 0.5$, the maximum depletion length is approximately equal to the second-foil thickness as shown in Fig. 8(g). We find that the electrons of the second-foil target will almost be separated from their equilibrium position to form the RES that is accelerated to the reflection direction, which ensures that only one electron sheet acts on the generation of the half-cycle AP in the transmission direction and results in a maximum charge separation field of $E_x \sim 100$ TV/m. Accordingly, the half-cycle AP generated by deceleration has the maximum intensity for $\beta = 0.5$.

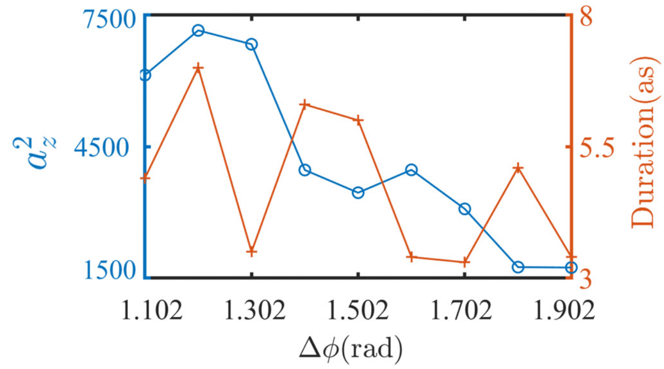

FIG. 9. Durations (attoseconds) at FWHM and normalized intensities a_z^2 of the AP as functions of relative phase $\Delta\phi$ between the two-color laser pulses in the case of optimal energy ratio $\beta = 0.5$.

In Fig. 9, we keep the phase $\phi_1 = 4.607$ rad of the fundamental-frequency laser pulse unchanged and change the phase ϕ_2 of the second-harmonic-frequency laser pulse to study the effect of the relative phase on AP production. As shown in Fig. 9, when the relative phase was within the range 1.102 rad $< \Delta\phi <$ 1.902 rad, the durations of the APs are all below 8 as, and the intensity decreases as the relative phase increases.

V. CONCLUSION

We highlight a regime of AP generation by the CBE regime. For laser pulses with normal incidence on a double-foil target, a giant half-cycle AP can be emitted in the CBE regime. The presence of a second foil target can control the motion of the relativistic electron nanobunch that is blown out from the first foil target to form the RFES. When the transmitted laser pulse has normal incidence on the second foil, it can pull the electrons out from the second foil to form the RES that is accelerated in the reflected direction, which results in a huge electrostatic field ∼100 TV/m. Accordingly, on the rear side of the second foil target, the RFES is decelerated rapidly by the huge electrostatic field, and bremsstrahlung emission occurs, which results in the generation of the half-cycle AP in the CBE regime.

The CBE regime of the half-cycle AP generation from the double-foil target scheme is robust, which is well verified with different laser and double-foil target conditions. As long as the normalized areal charge density is kept unchanged, the half-cycle AP can always be emitted in the CBE regime. The AP can still be effectively generated with only fundamental-frequency laser pulses with normal incidence on the double-foil target. The physical mechanism for the one-color laser pulse case is exactly the same as that of the two-color laser pulse case. However, the enhancement of the intensity of the half-cycle AP is achieved with the addition of the second-harmonic laser pulses.

The data that support the results of this study are available upon request from the authors.

ACKNOWLEDGMENTS

This research is supported by National Natural Science Foundation of China (NSFC; Grant No. 11974043). X.Y. acknowledges support by the National Natural Science Foundation of China (NSFC; Grant No. 11921006) and the National Grand Instrument Project (Grant No. 2019YFF01014400). The work of B.E. was carried out partially within the framework of the EUROfusion Consortium.

[1] T. Pfeifer, C. Spielmann, and G. Gerber, Rep. Prog. Phys. **69**, 443 (2006).
[2] F. Krausz and M. Ivanov, Rev. Mod. Phys. **81**, 163 (2009).
[3] P. B. Corkum and F. Krausz, Nat. Phys. **3**, 381 (2007).
[4] U. Teubner and P. Gibbon, Rev. Mod. Phys. **81**, 445 (2009).
[5] F. Quere, C. Thaury, P. Monot, S. Dobosz, P. Martin, J. P. Geindre, and P. Audebert, Phys. Rev. Lett. **96**, 125004 (2006).
[6] B. Dromey, S. Rykovanov, M. Yeung, R. Hörlein, D. Jung, D. C. Gautier, T. Dzelzainis, D. Kiefer, S. Palaniyppan, R. Shah, J. Schreiber, H. Ruhl, J. C. Fernandez, C. L. S. Lewis, M. Zepf, and B. M. Hegelich, Nat. Phys. **8**, 804 (2012).
[7] D. Kiefer, M. Yeung, T. Dzelzainis, P. S. Foster, S. G. Rykovanov, C. L. S. Lewis, R. S. Marjoribanks, H. Ruhl, D. Habs, J. Schreiber, M. Zepf, and B. Dromey, Nat. Commun. **4**, 1763 (2013).
[8] F. Y. Li, Z. M. Sheng, M. Chen, L. L. Yu, J. Meyer-ter-Vehn, W. B. Mori, and J. Zhang, Phys. Rev. E **90**, 043104 (2014).
[9] D. an der Brügge and A. Pukhov, Phys. Plasmas **17**, 033110 (2010).
[10] A. Pukhov and D. an der Brügge, and I. Kostyukov, Plasma Phys. Controlled Fusion **52**, 124039 (2010).
[11] M. Cherednychek and A. Pukhov, Phys. Plasmas **23**, 103301 (2016).
[12] B. Dromey, S. Cousens, S. Rykovanov, M. Yeung, D. Jung, D. C. Gautier, T. Dzelzainis, D. Kiefer, S. Palaniyppan, R. Shah, J. Schreiber, J. C. Fernandez, C. L. S. Lewis, M. Zepf, and B. M. Hegelich, New J. Phys. **15**, 015025 (2013).
[13] J. M. Mikhailova, M. V. Fedorov, N. Karpowicz, P. Gibbon, V. T. Platonenko, A. M. Zheltikov, and F. Krausz, Phys. Rev. Lett. **109**, 245005 (2012).
[14] S. Cousens, B. Reville, B. Dromey, and M. Zepf, Phys. Rev. Lett. **116**, 083901 (2016).
[15] S. Wei, Y. Wang, X. Yan, and B. Eliasson, Phys. Rev. E **106**, 025203 (2022).
[16] S. X. Hu and L. A. Collins, Phys. Rev. Lett. **96**, 073004 (2006).
[17] F. Krausz, Phys. Scr. **91**, 063011 (2016).
[18] M. Chini, K. Zhao, and Z. Chang, Nat. Photonics **8**, 178 (2014).
[19] G. Sansone, L. Poletto, and M. Nisoli, Nat. Photonics **5**, 655 (2011).
[20] M. Chini, B. Zhao, H. Wang, Y. Cheng, S. X. Hu, and Z. Chang, Phys. Rev. Lett. **109**, 073601 (2012).
[21] M. Yeung, B. Dromey, S. Cousens, T. Dzelzainis, D. Kiefer, J. Schreiber, J. H. Bin, W. Ma, C. Kreuzer, J. Meyer-ter-Vehn, M. J. V. Streeter, P. S. Foster, S. Rykovanov, and M. Zepf, Phys. Rev. Lett. **112**, 123902 (2014).
[22] M. Yeung, J. Bierbach, E. Eckner, S. Rykovanov, S. Kuschel, A. Sävert, M. Förster, C. Rödel, G. G. Paulus, S. Cousens, M. Coughlan, B. Dromey, and M. Zepf, Phys. Rev. Lett. **115**, 193903 (2015).
[23] R. Lichters, J. Meyer-ter-Vehn, and A. Pukhov, Phys. Plasmas **3**, 3425 (1996).
[24] T. Baeva, S. Gordienko, and A. Pukhov, Phys. Rev. E **74**, 065401(R) (2006).
[25] S. G. Rykovanov, M. Geissler, J. Meyer-ter-Vehn, and G. D. Tsakiris, New J. Phys. **10**, 025025 (2008).
[26] P. Heissler, R. Hörlein, M. Stafe, J. M. Mikhailova, Y. Nomura, D. Herrmann, R. Tautz, S. G. Rykovanov, I. B. Földes, K. Varjú, F. Tavella, A. Marcinkevicius, F. Krausz, L. Veisz, and G. D. Tsakiris, Appl. Phys. B **101**, 511 (2010).
[27] J. H. Easter, J. A. Nees, B. X. Hou, A. Mordovanakis, G. Mourou, A. G. R. Thomas, and K. Krushelnick, New J. Phys. **15**, 025035 (2013).
[28] C. Altucci, R. Velotta, V. Tosa, P. Villoresi, F. Frassetto, L. Poletto, C. Vozzi, F. Calegari, M. Negro, S. De Silvestri, and S. Stagira, Opt. Lett. **35**, 2798 (2010).
[29] A. Jullien, T. Pfeifer, M. J. Abel, P. M. Nagel, M. J. Bell, D. M. Neumark, and S. R. Leone, Appl. Phys. B **93**, 433 (2008).
[30] Y. X. Zhang, S. Rykovanov, M. Shi, C. L. Zhong, X. T. He, B. Qiao, and M. Zepf, Phys. Rev. Lett. **124**, 114802 (2020).
[31] Y. Jiang, Z.-Y. Chen, Z. Liu, L. Cao, C. Zheng, R. Xie, Y. Chao, and X. He, Opt. Lett. **46**, 1285 (2021).
[32] Y. Shou, R. Hu, Z. Gong, J. Yu, J. Chen, G. Mourou, X. Yan, and W. Ma, New J. Phys. **23**, 053003 (2021).
[33] G. D. Tsakiris, K. Eidmann, J. Meyer-ter-Vehn, and F. Krausz, New J. Phys. **8**, 19 (2006).

[34] X. R. Xu, B. Qiao, H. X. Chang, Y. X. Zhang, H. Zhang, C. L. Zhong, C. T. Zhou, S. P. Zhu, and X. T. He, Plasma Phys. Controlled Fusion **60**, 045005 (2018).
[35] X. Xu, Y. Zhang, H. Zhang, H. Lu, W. Zhou, C. Zhou, B. Dromey, S. Zhu, M. Zepf, X. He, and B. Qiao, Optica **7**, 355 (2020).
[36] H. C. Wu and J. Meyer-ter-Vehn, Nat. Photonics **6**, 304 (2012).
[37] W. J. Ma, J. H. Bin, H. Y. Wang, M. Yeung, C. Kreuzer, M. Streeter, P. S. Foster, S. Cousens, D. Kiefer, B. Dromey, X. Q. Yan, J. Meyer-ter-Vehn, M. Zepf, and J. Schreiber, Phys. Rev. Lett. **113**, 235002 (2014).
[38] A. Pakhomov, M. Arkhipov, N. Rosanov, and R. Arkhipov, Phys. Rev. A **105**, 043103 (2022).
[39] X. X. Dong, Y. R. Liu, V. Kimberg, O. Vendrell, Y. Wu, J. G. Wang, J. Chen, and S. B. Zhang, Commun. Phys. **5**, 181 (2022).
[40] A. S. Moskalenko, Z.-G. Zhu, and J. Berakdar, Phys. Rep. **672**, 1 (2017).
[41] T. D. Arber, K. Bennett, C. S. Brady, A. Lawrence-Douglas, M. G. Ramsay, N. J. Sircombe, P. Gillies, R. G. Evans, H. Schmitz, A. R. Bell, and C. P. Ridgers, Plasma Phys. Controlled Fusion **57**, 113001 (2015).
[42] B. Qiao, M. Zepf, M. Borghesi, B. Dromey, and M. Geissler, New J. Phys. **11**, 103042 (2009).
[43] R. Pang, Y. Wang, X. Yan, and B. Eliasson, Phys. Rev. Appl. **18**, 024024 (2022).
[44] S. V. Bulanov, T. Zh. Esirkepov, M. Kando, S. S. Bulanov, S. G. Rykovanov, and F. Pegoraro, Phys. Plasmas **20**, 123114 (2013).
[45] A. S. Moskalenko, A. Matos-Abiague, and J. Berakdar, Phys. Rev. B **74**, 161303(R) (2006).